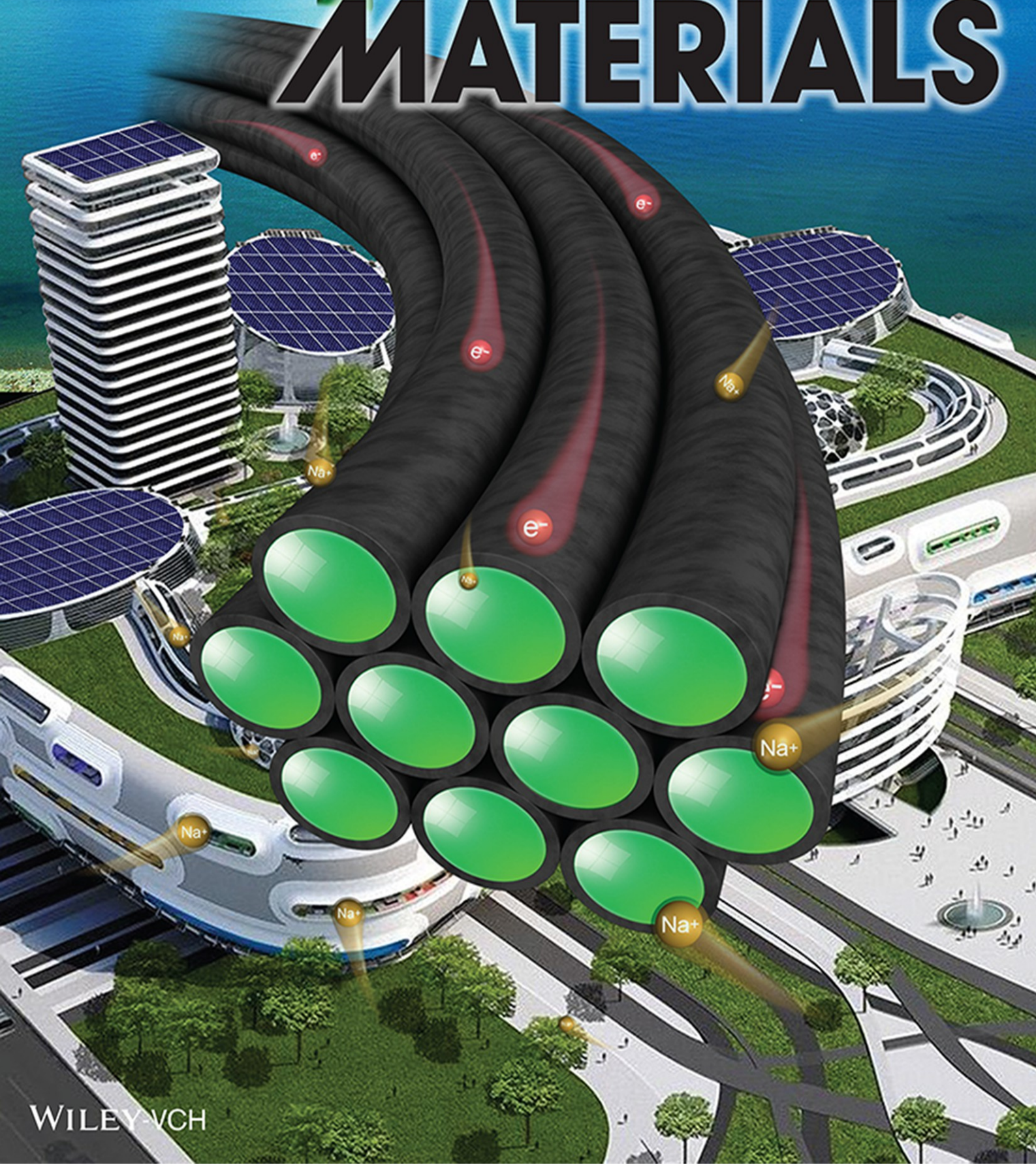


Vol. 5 • No. 17 • September 9 • 2015

www.advenergymat.de

ADVANCED ENERGY MATERIALS



WILEY-VCH

Novel $K_3V_2(PO_4)_3/C$ Bundled Nanowires as Superior Sodium-Ion Battery Electrode with Ultrahigh Cycling Stability

Xuanpeng Wang, Chaojiang Niu, Jiashen Meng, Ping Hu, Xiaoming Xu, Xiujuan Wei, Liang Zhou,* Kangning Zhao, Wen Luo, Mengyu Yan, and Liqiang Mai*

Sodium-ion battery has captured much attention due to the abundant sodium resources and potentially low cost. However, it suffers from poor cycling stability and low diffusion coefficient, which seriously limit its widespread application. Here, $K_3V_2(PO_4)_3/C$ bundled nanowires are fabricated using a facile organic acid-assisted method. With a highly stable framework, nanoporous structure, and conductive carbon coating, the $K_3V_2(PO_4)_3/C$ bundled nanowires manifest excellent electrochemical performances in sodium-ion battery. A stable capacity of 119 mAh g^{-1} can be achieved at 100 mA g^{-1} . Even at a high current density of 2000 mA g^{-1} , 96.0% of the capacity can be retained after 2000 charge–discharge cycles. Comparing with $K_3V_2(PO_4)_3/C$ blocks, the $K_3V_2(PO_4)_3/C$ bundled nanowires show significantly improved cycling stability. This work provides a facile and effective approach to enhance the electrochemical performance of sodium-ion batteries.

1. Introduction

With the development of renewable energy sources such as solar and wind, we are facing the significant challenge of integrating them into the grid.^[1] Thus, it is an urgent demand to develop large-scale energy storage systems with high capacity, long life, high safety, and low cost for grid utilization.^[2,3] Among the various energy storage technologies, battery is the best candidate for storing electricity in the form of chemical energy due to its dexterity, convenience, and high-energy conversion efficiency.^[4–6] Owing to its high energy density, lithium-ion battery has expanded its application from portable electronics to electric vehicles (EV) and hybrid electric vehicles (HEV).^[7–10] However, lithium is not an abundant element and the increasing cost has limited its widespread large-scale application. By contrast, sodium is optimistically abundant in nature (ranking fourth among the most abundant elements in the earth crust) and fairly low in cost. In addition, sodium

is located below lithium in the periodic table and shares similar physical/chemical properties with lithium in many aspects. Thus, sodium is a promising candidate for replacing lithium in energy storage systems.^[11] Recently, sodium ion batteries have been widely reconsidered for large-scale applications. Undoubtedly, the exploration and development of sodium-ion batteries is a new and important direction in the field of energy storage.

Recently, potassium containing compounds have been investigated in sodium-ion batteries. Liu et al. found that the potassium ion intercalated manganese oxide ($K_{0.27}MnO_2$) with large ion diffusion channels shows superior cycling stability and rate capability for sodium storage.^[12] This inspiring work indicates

that the potassium-containing compounds have great potentials in energy storage. On the other hand, phosphates have been widely studied because of their high redox potential, good safety, and low cost. Compared with metal oxides, phosphates possess higher electrochemical voltage and thus higher energy density due to the inductive effect of PO_4^{3-} .^[4,5] In addition, the phosphates also provide higher thermal stability for elevated temperature operation. However, the phosphates face the defects of regular impure phase and poor electronic conductivity.^[4,5] The formation of impurity phases can be suppressed by thoroughly mixing the reactants before sintering, and the conductivity can be improved by compositing with carbon.^[13–19] Among the phosphate compounds, $Li_3V_2(PO_4)_3$ ^[20,21] and $Na_3V_2(PO_4)_3$ ^[22–25] have been widely studied as lithium or sodium-ion battery cathodes. For example, Jian et al. reported the synthesis of $Na_3V_2(PO_4)_3/C$ composite by a one-step solid state reaction; when used as the cathode for sodium-ion battery, it delivers an initial discharge capacity of 93 mAh g^{-1} .^[23] Saravanan et al. reported the preparation of porous $Na_3V_2(PO_4)_3/C$ with excellent cycling stability and superior rate capability in sodium-ion battery.^[25] Despite the numerous reports on $Li_3V_2(PO_4)_3$ and $Na_3V_2(PO_4)_3$, the crystal structure and electrochemical performance of $K_3V_2(PO_4)_3$ has never been reported.

Herein, a novel potassium containing phosphate material, $K_3V_2(PO_4)_3$, is designed and explored in energy storage. The $K_3V_2(PO_4)_3/C$ bundled nanowires were synthesized by a facile organic acid-assisted method. With a highly stable framework for sodium storage, porous nanostructure for fast

Dr. X. Wang, Dr. C. Niu, Dr. J. Meng, Dr. P. Hu,
Dr. X. Xu, Dr. X. Wei, Prof. L. Zhou, Dr. K. Zhao,
Dr. W. Luo, Dr. M. Yan, Prof. L. Mai
State Key Laboratory of Advanced Technology
for Materials Synthesis and Processing
Wuhan University of Technology
Wuhan 430070, China
E-mail: liangzhou@whut.edu.cn; mlq518@whut.edu.cn



DOI: 10.1002/aenm.201500716

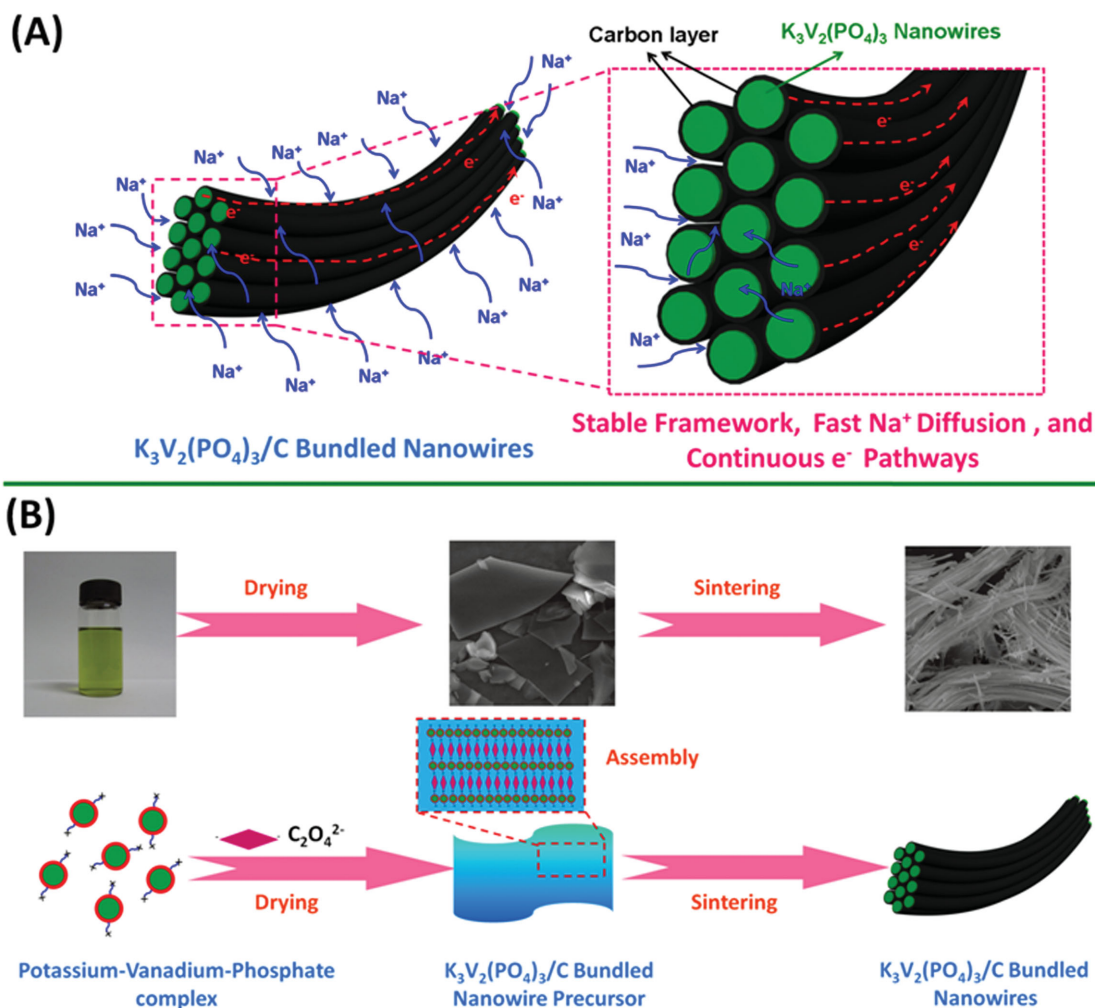


Figure 1. A) Schematic illustration of the $K_3V_2(PO_4)_3/C$ bundled nanowires with stable framework, fast Na^+ diffusion, and high electronic conductivity. B) Schematic illustration for the fabrication process and proposed formation mechanism of the $K_3V_2(PO_4)_3/C$ bundled nanowires.

sodium ion diffusion, and conductive carbon coating for rapid electron transport (Figure 1A), the $K_3V_2(PO_4)_3/C$ bundled nanowires manifest excellent electrochemical performances in sodium-ion battery. When used as the cathode material, the $K_3V_2(PO_4)_3/C$ bundled nanowires exhibit an initial capacity of 119 mAh g^{-1} with a superior capacity retention of 99.4% after 100 cycles at 100 mA g^{-1} . Even after 2000 cycles at a high rate of 2000 mA g^{-1} , 96.0% of the initial capacity can be retained. Such a facile and energy-saving strategy for constructing bundled carbon-coated nanowires may be extended to the synthesis of other active materials for energy storage applications.

2. Results and Discussions

2.1. Formation Mechanism of $K_3V_2(PO_4)_3/C$ Bundled Nanowires

In this work, the $K_3V_2(PO_4)_3/C$ bundled nanowires are synthesized via a facile organic acid-assisted method (Figure 1B

and Figure S1, Supporting Information), which contains three main steps. (I) V(V) reduction in solution: NH_4VO_3 , KOH, and phosphoric acid were dissolved in deionized water to form a maroon solution. Oxalic acid ($C_2H_2O_4 \cdot 2H_2O$) was then added. After stirring for 4 h, the color of the solution turned into yellowish green, indicating the partial reduction of V(V) to V(IV) by the oxalic acid ($2 H^+ + 2 VO_3^- + 3 C_2H_2O_4 \cdot 2H_2O = 2 VO^{2+} + 2 C_2O_4^{2-} + 2 CO_2 + 10 H_2O$; Figure S2A, Supporting Information). (II) Organic acid-assisted assembly: the solution was poured into a Petri dish, dried (solvent evaporation) at $60 \text{ }^\circ\text{C}$, and baked at $180 \text{ }^\circ\text{C}$ to form sponge-like solids with plate-like morphology (Figures S1, S2C, Supporting Information). During the solvent evaporation, the excess amount of oxalic acid distributed at the interstitial space of potassium–vanadium–phosphate complex and acted as the structure directing agent. Namely, the potassium–vanadium–phosphate complex is surrounded by the oxalic acid (Figure 1B). (III) In situ crystallization and carbon coating: the as-prepared sponge-like precursor containing potassium, vanadium, phosphate, and oxalic

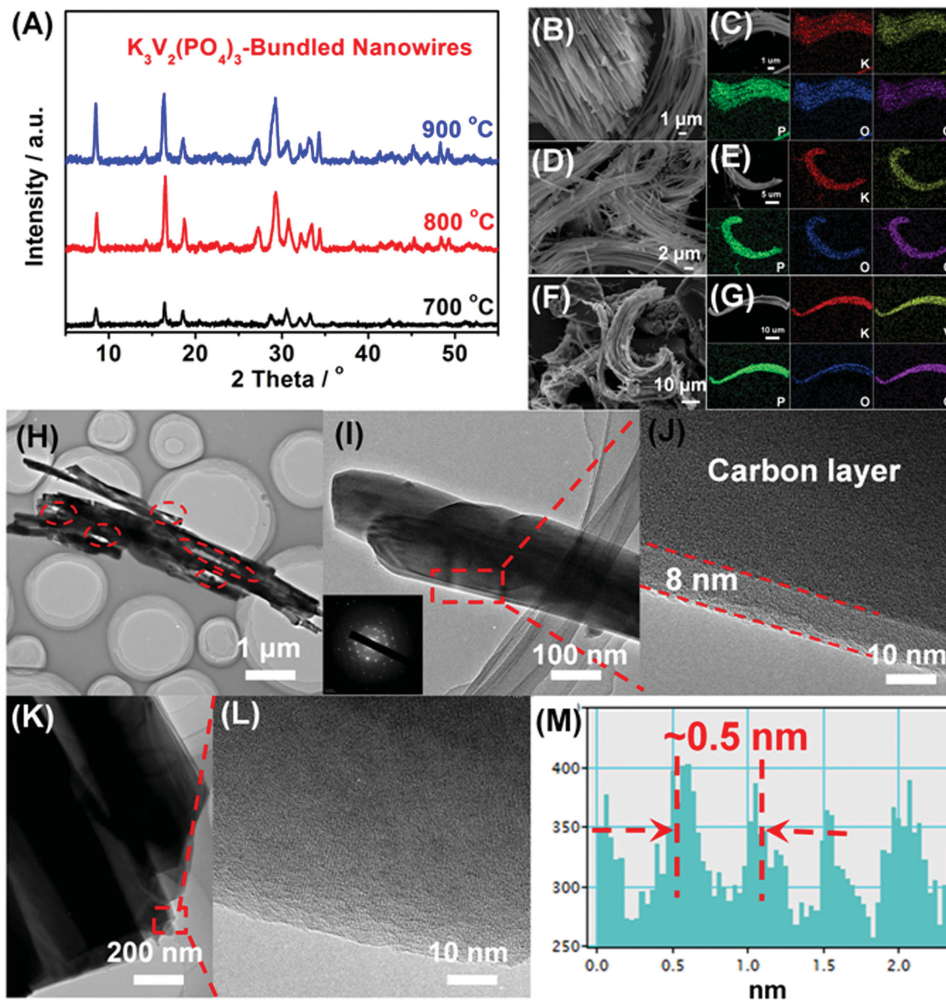


Figure 2. XRD patterns A) of the $\text{K}_3\text{V}_2(\text{PO}_4)_3/\text{C}$ bundled nanowires sintered at 700, 800, and 900 °C. SEM image B) and elemental mapping images C) of the bundled nanowires sintered at 700 °C. SEM image D) and elemental mapping images E) of the bundled nanowires sintered at 800 °C. SEM image F) and elemental mapping images G) of the bundled nanowires sintered at 900 °C. TEM images H–K) and HRTEM image L) of the $\text{K}_3\text{V}_2(\text{PO}_4)_3/\text{C}$ bundled nanowires sintered at 800 °C. Inset of (I) is the SAED pattern of the bundled nanowires. The interplanar spacing M) of the $\text{K}_3\text{V}_2(\text{PO}_4)_3/\text{C}$ bundled nanowires.

acid was decomposed into $\text{K}_3\text{V}_2(\text{PO}_4)_3/\text{C}$. During the annealing, the oxalic acid played two roles. On one hand, it acted as the carbon precursor, confining the growth of $\text{K}_3\text{V}_2(\text{PO}_4)_3$; on the other hand, it acted as the structure directing agent, promoting the formation of $\text{K}_3\text{V}_2(\text{PO}_4)_3/\text{C}$ bundled nanowires. If the solution obtained from step I was continuously stirred for another 8 h, more V(V) was reduced to V(IV), which can be indicated from the dark blue color of the solution (Figure S2B, Supporting Information).^[26–29] Meanwhile, more oxalic acid was consumed. Due to the less amount of oxalic acid remaining in the solution/precursor, it was not enough to act as the structure directing agent. As a result, $\text{K}_3\text{V}_2(\text{PO}_4)_3/\text{C}$ blocks rather than bundled nanowires were obtained after drying, baking, and sintering (Figure S2D, Supporting Information).

2.2. Structure Characterization

X-ray diffraction (XRD) patterns of the samples prepared at 700, 800, and 900 °C clearly indicate the formation of a highly

crystalline phase (Figure 2A). No diffraction peaks originated from carbon are discerned, indicating the amorphous feature of carbon.^[30,31] It should be mentioned that the XRD pattern cannot be indexed to any known phase from the existing JCPDS database, suggesting the formation of a possible new crystalline phase. However, the detailed structure of this possible new phase is still under study. When the sintering temperature is below 800 °C, the bundled nanowire morphology can be well kept (Figure 2B–E). When the temperature is increased to 900 °C, the bundled nanowire morphology is partially destroyed (Figure 2F,G). Inductively coupled plasma (ICP) results show that the molar ratio of K:V:P is close to 3:2:3 for all samples (Table S1, Supporting Information). Elemental mapping results demonstrate the uniform distribution of K, V, P, O, and C (Figure 2C,E,G). By combining the XRD, ICP, and elemental mapping results together, the obtained products are tentatively assigned to $\text{K}_3\text{V}_2(\text{PO}_4)_3/\text{C}$.

Scanning electron microscopy (SEM) and transmission electron microscopy (TEM) are utilized to elucidate the detailed

structure of the bundled nanowires (Figure 2H,I and Figure S4, Supporting Information). The length of individual nanowire is in the range of 5–30 μm , and the diameter is in the range of 150–500 nm. It should be mentioned that the nanowires tend to aggregate into bundles and the diameter of the bundled nanowires may reach 1–5 μm . The $\text{K}_3\text{V}_2(\text{PO}_4)_3$ nanowire is quasi-single-crystalline, as can be indicated from the selected area electron diffraction (SAED) pattern (inset of Figure 2I). A thin carbon layer with a thickness of ≈ 8 nm can be observed on the surface of the $\text{K}_3\text{V}_2(\text{PO}_4)_3$ nanowire (Figure 2J). High-resolution TEM (HRTEM) images of the $\text{K}_3\text{V}_2(\text{PO}_4)_3/\text{C}$ nanowires (Figure 2K–M) display a lattice fringe of ≈ 0.5 nm.

XRD patterns of the $\text{K}_3\text{V}_2(\text{PO}_4)_3/\text{C}$ blocks are illustrated in Figure S5 (Supporting Information), which resembles that of the nanowires. ICP test shows that the molar ratio of K:V:P is close to 3:2:3, in line with the feeding ratio (Table S2, Supporting Information). SEM images show that the $\text{K}_3\text{V}_2(\text{PO}_4)_3/\text{C}$ blocks are porous in nature, with macropores randomly distributed throughout the whole particle (Figure S6, Supporting Information). Elemental mapping results show that the K, V, P, O, and C distribute homogeneously in the blocks (Figure S7, Supporting Information).

Raman spectroscopy is employed to study the nature of the in situ formed carbon in the $\text{K}_3\text{V}_2(\text{PO}_4)_3/\text{C}$ composites (Figure S8A, Supporting Information). The characteristic peaks located at around 1600 and 1350 cm^{-1} can be attributed to the G-band (graphitic carbon) and D-band (originating from disordered carbon) of carbon, respectively. For all samples, the intensity of G-band is comparable to that of D-band, indicating the partially graphitized feature of carbon.^[32,33] Fourier-transform infrared spectroscopy (FT-IR) is carried out (Figure S8B, Supporting Information) to gain more structural information. All samples exhibit similar absorption bands in FTIR, suggesting their similar structure. Specifically, the absorption band at 1630 cm^{-1} can be attributed to the –OH stretching vibration of absorbed H_2O ;^[34] the bands located at 936, 997, 1106, and 1165 cm^{-1} can be assigned to the P–O stretching vibrations;^[35] the band centered at 878 cm^{-1} can be ascribed to the V–O stretching vibrations;^[36] the bands at 482, 540, 562, and 667 cm^{-1} can be assigned to O–P–O bending vibrations.^[37] Thermo gravimetric analysis (TGA) curves of $\text{K}_3\text{V}_2(\text{PO}_4)_3/\text{C}$ bundled nanowires and blocks are shown in Figure S9 (Supporting Information). The TGA curves show that the mass decreases with the increase of temperature before 500 $^\circ\text{C}$, and then increases with the temperature from 500 to 900 $^\circ\text{C}$. The weight loss before 500 $^\circ\text{C}$ is caused by the combustion of carbon, while the weight gain after 500 $^\circ\text{C}$ is attributed to the oxidation of V(III) to V(IV) and V(V). The carbon content of the bundled nanowires and blocks is measured to be $\approx 6.0\%$ and $\approx 8.0\%$, respectively. X-ray photoelectron spectroscopy (XPS) is conducted to study the chemical state of vanadium (Figure S10, Supporting Information). The V 2p_{3/2} core level region shows a single peak with a binding energy (BE) of 517.2 eV, which is associated with the V^{3+} oxidation state. The BE also matches well with that observed in V_2O_3 (517.3 eV).^[38–40] The XPS characterization also suggests the chemical composition of $\text{K}_3\text{V}_2(\text{PO}_4)_3$, highly consistent with the XRD, EDS, SAED, and ICP results.

The specific surface area and pore size distribution of the $\text{K}_3\text{V}_2(\text{PO}_4)_3/\text{C}$ are tested by nitrogen sorption. The bundled nanowires present a typical hysteresis loop for porous materials

at high relative pressures (Figure S11, Supporting Information). The Brunauer–Emmett–Teller (BET) surface area is calculated to be 44.0 $\text{m}^2 \text{g}^{-1}$ (Figure S11A, Supporting Information), which is 13 times higher than that of the blocks (3.3 $\text{m}^2 \text{g}^{-1}$; Figure S11B, Supporting Information). The $\text{K}_3\text{V}_2(\text{PO}_4)_3/\text{C}$ bundled nanowires exhibit a single pore size distribution, with the peak centered at ≈ 21 nm (inset of Figure S11A in the Supporting Information), while the $\text{K}_3\text{V}_2(\text{PO}_4)_3/\text{C}$ blocks exhibit no obviously peak in the pore size distribution (inset of Figure S11B in the Supporting Information). The high specific surface area and pore volume (0.17 $\text{cm}^3 \text{g}^{-1}$) of the bundled nanowires are attributed to the existence of cracks/pores (Figure 2H).

2.3. Ex Situ and In Situ XRD Analysis

To study the structural stability of the $\text{K}_3\text{V}_2(\text{PO}_4)_3/\text{C}$ bundled nanowires during sodiation/desodiation, in situ and ex situ XRD are performed. For the in situ XRD, the half cell is galvanostatically charged and discharged for two cycles at 100 mA g^{-1} (Figure 3A, Figure S12, Supporting Information). Only tiny changes can be observed at 23–27 $^\circ$ and 30–34 $^\circ$, indicating the

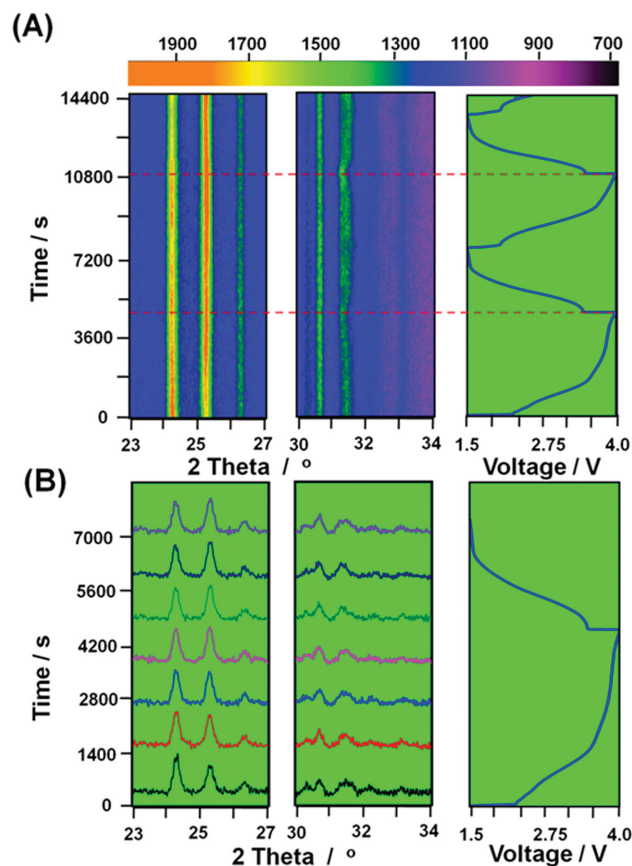


Figure 3. In situ XRD patterns during galvanostatic charge and discharge at 100 mA g^{-1} . A) The image plot of the diffraction patterns at 23–27 $^\circ$ and 30–34 $^\circ$ during the first two charge–discharge cycles. The horizontal axis represents the selected 2θ regions, and time is on the vertical axis. The diffraction intensity is color coded with the scale bar shown on the top. The corresponding voltage curve is plotted to the right. B) Selected diffraction patterns during the first cycle stacked against the voltage profile.

slight variation of the lattice parameters during the charge–discharge.^[41,42] In the first charge process, the peak centered at 24.2° weakens and the peak centered at 25.2° strengthens, which are caused by the extraction of K⁺. This trend is reversed during the first discharge process, corresponding to the insertion of K⁺/Na⁺ (Figure 3B). Interestingly, the peak located at 31.4° exhibits a slight shift toward low angle at the end of charge, and it shift back to its original position in the subsequent discharge process, indicating a reversible expansion/extraction of the corresponding lattice distance.^[43,44] The slight shift and intensity variation in diffraction peaks in the process of in situ characterization indicate that there is no severe structural change in the process of K⁺/Na⁺ insertion/extraction, confirming the highly stable framework of K₃V₂(PO₄)₃.^[45,46] Ex situ XRD results provide insights into the long-term structural stability of the K₃V₂(PO₄)₃. No obvious change can be observed in the ex situ XRD patterns (Figure S13, Supporting Information, 6.5–10.5°), except for the slight right-shift of the diffraction peak. Due to the extraction of the large K⁺ from the K₃V₂(PO₄)₃ framework, the cell contracts along certain directions.^[41] As a result, the diffraction peak shifts from 8.5° to 9.0° during the first charge. Even after 500 charge–discharge cycles, the diffraction peak can be well maintained at 9.0°, suggesting the high stability of the K₃V₂(PO₄)₃ framework. By combining the in situ and ex situ XRD results together, it can be concluded that the framework of K₃V₂(PO₄)₃/C bundled nanowires is robust enough to tolerate the K⁺/Na⁺ insertion/extraction.

2.4. Electrochemical Performance of Bundled Nanowires and Blocks

To study the theoretical capacity of K₃V₂(PO₄)₃, the galvanostatic intermittent titration technique (GITT) test is conducted (Figure S14, Supporting Information). The K₃V₂(PO₄)₃ bundled nanowires show a theoretical charge capacity of 174 mAh g⁻¹, corresponding to the extraction of 3.3 Na⁺/K⁺ per formula. It is noted that the K₃V₂(PO₄)₃ contains only three K⁺; however, 3.3 Na⁺/K⁺ can be extracted. To explain this discrepancy, ex situ ICP test is conducted. The ex situ ICP results show that 0.8 Na⁺ is preintercalated from the electrolyte into the K₃V₂(PO₄)₃ before charging (Table S3, Supporting Information). During the charge, 0.8 Na⁺ and 2.5 K⁺ are extracted from the presodiated K₃V₂(PO₄)₃. The theoretical discharge capacity of charged K₃V₂(PO₄)₃ is 159 mAh g⁻¹, corresponding to the insertion of 3.0 Na⁺ per formula.

The sodium storage performance of the K₃V₂(PO₄)₃/C samples is then investigated by cyclic voltammograms (CV) and galvanostatic charge–discharge tests. The CV curves (Figure 4A) and *dq/dv* plots (Figure S15, Supporting Information) of the K₃V₂(PO₄)₃/C bundled nanowires and blocks share the same characteristics with two pairs of cathodic/anodic peaks. In the first anodic process, two oxidation peaks are located at 1.55 and 3.61 V. In the subsequent cathodic process, two reduction peaks appear at 3.65 and 1.75 V. Obviously, the K₃V₂(PO₄)₃/C bundled nanowires have larger curve area and higher redox peak current than the K₃V₂(PO₄)₃/C blocks, indicating the higher capacity and faster kinetics for Na⁺ insertion/extraction.

Figure S16 (Supporting Information) shows the cycling and rate performances of the three nanowire samples prepared at

different sintering temperatures. Among the three samples, the sample prepared at 800 °C exhibits the best electrochemical performance. Thus, 800 °C is considered to be the optimized sintering temperature. Representative charge–discharge curves of the K₃V₂(PO₄)₃/C bundled nanowires at 100 mA g⁻¹ are presented in Figure 4B. Two weak discharge plateaus can be observed at around 1.6 and 3.6 V, in agreement with the CV results.

The electrochemical performances of the K₃V₂(PO₄)₃/C bundled nanowires and blocks are compared in Figure 4C–F. In general, the bundled nanowires manifest better cycling stability and rate capability than the blocks. At a current density of 100 mA g⁻¹, the bundled nanowires deliver an initial discharge capacity of 119 mAh g⁻¹, maintaining 118.2 mAh g⁻¹ after 100 cycles (capacity retention of 99.4%). The initial Coulombic efficiency is 73.8%. It increases gradually to 97.3% after 30 cycles and then can be stabilized at 98.0% (Figure S17, Supporting Information). The blocks deliver an initial capacity of 109 mAh g⁻¹ under the same current density, retaining 61.3 mAh g⁻¹ after 100 cycles (capacity retention of 56.2%). At 200 mA g⁻¹, the bundled nanowires show a stable capacity of ≈90 mAh g⁻¹ for 600 cycles (Figure 4D). In contrast, the capacity of the blocks decays to below 50 mAh g⁻¹ in 100 cycles. At 500 mA g⁻¹, the bundled nanowires can be charge–discharged for 1000 cycles with a capacity retention of 93.8% (Figure 4E).

When tested at various current densities ranging from 100 to 1000 mA g⁻¹, the bundled nanowires exhibit higher capacity at each current than the blocks, demonstrating the superior rate performance (Figure 4F; Figure S18, Supporting Information). When the current density is reduced from 1000 to 100 mA g⁻¹, ≈100% of the initial capacity can be recovered for the bundled nanowires, while only ≈63% of the initial capacity can be recovered for the blocks. The most appealing property of the bundled nanowires is their excellent cycling stability at high rate (Figure 4G). At a current density of 1000 mA g⁻¹, 99.0% of the initial capacity can be retained after 2000 cycles; at a current density of 2000 mA g⁻¹, 96.0% of the initial capacity can be retained after 2000 cycles. Compared to previous literatures on phosphate-based cathode materials for sodium-ion batteries, the cycling stability of the K₃V₂(PO₄)₃/C bundled nanowires is among the best (Table S4, Supporting Information). In sharp contrast to the bundled nanowires, the blocks exhibit very low capacity and poor cycling stability at high rate (Figure S19, Supporting Information).

The structural stability of the K₃V₂(PO₄)₃/C bundled nanowires and blocks is further studied by ex situ SEM and TEM (Figures S20–S22, Supporting Information). The structure of the bundled nanowires can be well maintained after 100 cycles at 100 mA g⁻¹ and 2000 cycles at 1000 mA g⁻¹ (Figures S20 and S21, Supporting Information). Although the morphology of the blocks can be generally maintained after 100 cycles at 100 mA g⁻¹, the size significantly decreases, which may be caused by the pulverization during cycling (Figures S22, Supporting Information).^[47,48] The better structural stability of the bundled nanowires than the blocks underpins their significant difference in cycling stability.

The apparent diffusion coefficients for semi-infinite diffusion of Na⁺ into K₃V₂(PO₄)₃ are calculated based on the Randles–Sevcik equation.^[49]

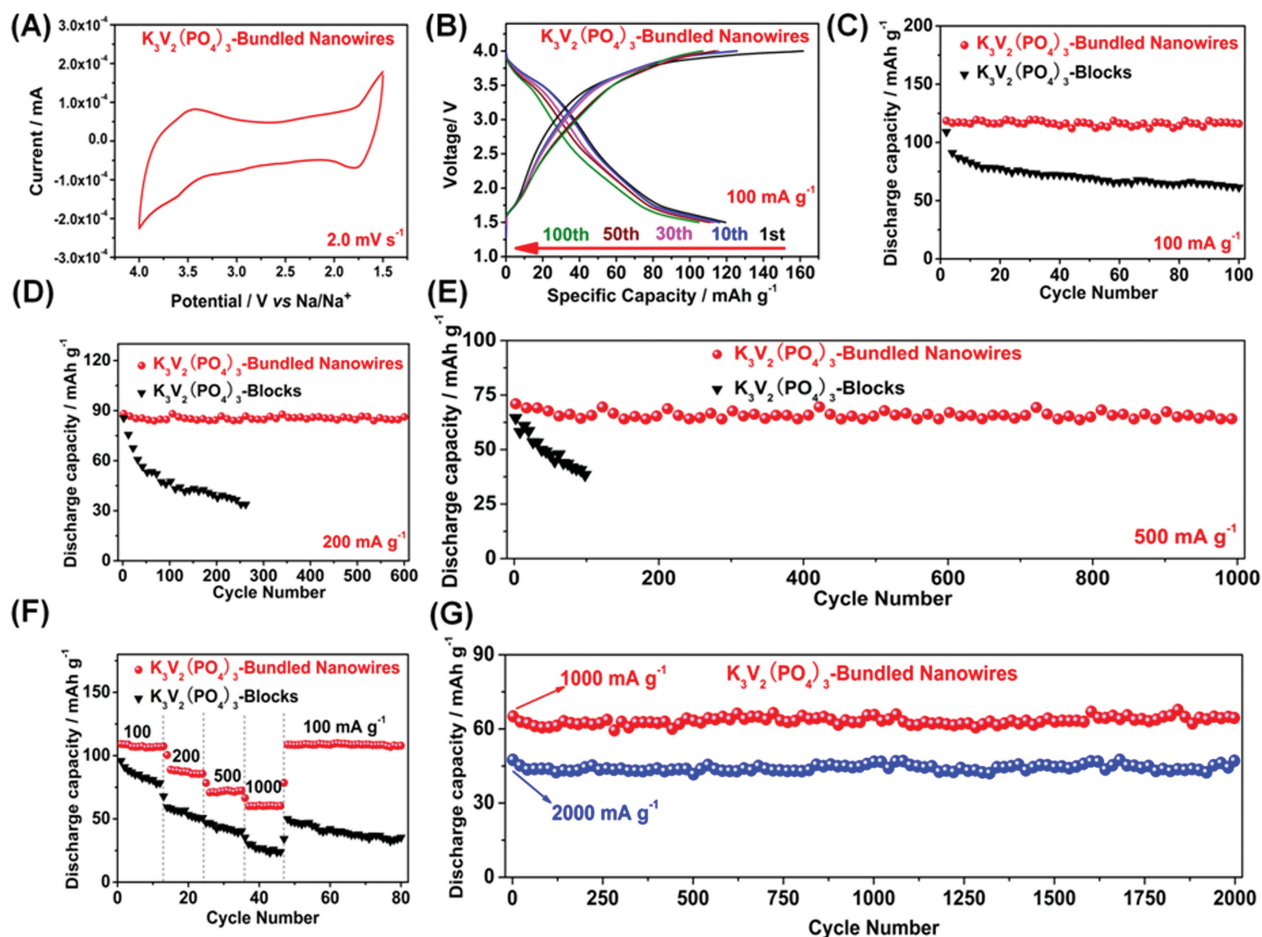


Figure 4. Electrochemical performances of the $\text{K}_3\text{V}_2(\text{PO}_4)_3/\text{C}$ bundled nanowires and $\text{K}_3\text{V}_2(\text{PO}_4)_3/\text{C}$ blocks sintered at 800°C in sodium-ion batteries: A) cyclic voltammograms (CV) of $\text{K}_3\text{V}_2(\text{PO}_4)_3/\text{C}$ bundled nanowires at a scan rate of 2 mV s^{-1} in the electrochemical window of $1.5\text{--}4.0\text{ V}$ versus Na/Na^+ . B) Charge–discharge curves at 100 mA g^{-1} . C–E) Cycling performance of the $\text{K}_3\text{V}_2(\text{PO}_4)_3/\text{C}$ bundled nanowires and blocks at $100, 200,$ and 500 mA g^{-1} in the electrochemical window of $1.5\text{--}4.0\text{ V}$. F) Rate performance of the $\text{K}_3\text{V}_2(\text{PO}_4)_3/\text{C}$ bundled nanowires and blocks. G) Long-life cycling performance of the $\text{K}_3\text{V}_2(\text{PO}_4)_3/\text{C}$ bundled nanowires at 1000 and 2000 mA g^{-1} .

$$I_p = 0.4463n\text{ FAC} \left(\frac{NFvD}{RT} \right)^{1/2} = [269\,000 \times n^{3/2}AD^{1/2}C]v^{1/2} \quad (1)$$

where I_p is the peak current, n is the number of electrons transferred per molecule during the electrochemical reaction (here 1), A is the active surface area of the electrode (here $3.752 \times \pi\text{ mm}^2$), C is the concentration of sodium ions in the cathode (here 1), D is the apparent Na^+ diffusion coefficient of the whole electrode involving the diffusion of both sodium ions and electrons, and v is the scanning rate. From the slope of the fitting line collected from the peak c (Figure 5A and Figure S23A, Supporting Information), the apparent diffusion coefficients D of the bundled nanowires are determined to be $1.6 \times 10^{-8}\text{ cm}^2\text{ s}^{-1}$ (Figure 5B), which is 4.0 times higher than that of the blocks ($4.0 \times 10^{-9}\text{ cm}^2\text{ s}^{-1}$) (Figure S23B, Supporting Information) and 10^4 times higher than that of $\text{Na}_3\text{V}_2(\text{PO}_4)_3/\text{AC}$ ($1.51 \times 10^{-12}\text{ cm}^2\text{ s}^{-1}$).^[11] The Nyquist plots indicate that the charge transfer resistance (R_{ct}) of the bundled nanowires is only $84\ \Omega$ before cycling, lower than that of the blocks

($182\ \Omega$) (Figure 5C). After 100 cycles at 100 mA g^{-1} , the R_{ct} of the bundled nanowires is $90\ \Omega$, while that of the blocks is $312\ \Omega$ (Figure 5D), suggesting the fast electronic mobility of the bundled nanowires. The diffusion coefficient and EIS results indicate that the constructed $\text{K}_3\text{V}_2(\text{PO}_4)_3/\text{C}$ bundled nanowires can enhance the ionic transport kinetics and electronic conductivity, leading to better rate capability than the blocks.

The remarkable electrochemical properties of the $\text{K}_3\text{V}_2(\text{PO}_4)_3/\text{C}$ bundled nanowires can be attributed to their unique structural features and crystal structure. First, the $\text{K}_3\text{V}_2(\text{PO}_4)_3$ possesses a highly stable framework, which is beneficial to the cycling stability. Second, the $\text{K}_3\text{V}_2(\text{PO}_4)_3/\text{C}$ bundled nanowires exhibit a considerable amount of porosity, resulting in rapid Na^+ diffusion and thus high rate capability. Third, the surface carbon coating on the bundled nanowires improves the conductivity of the nanocomposite, and further boosts the electrochemical reaction kinetics (rate performance). The surface carbon layer can also prevent the aggregation of the nanowires and guarantees the effective electron contact

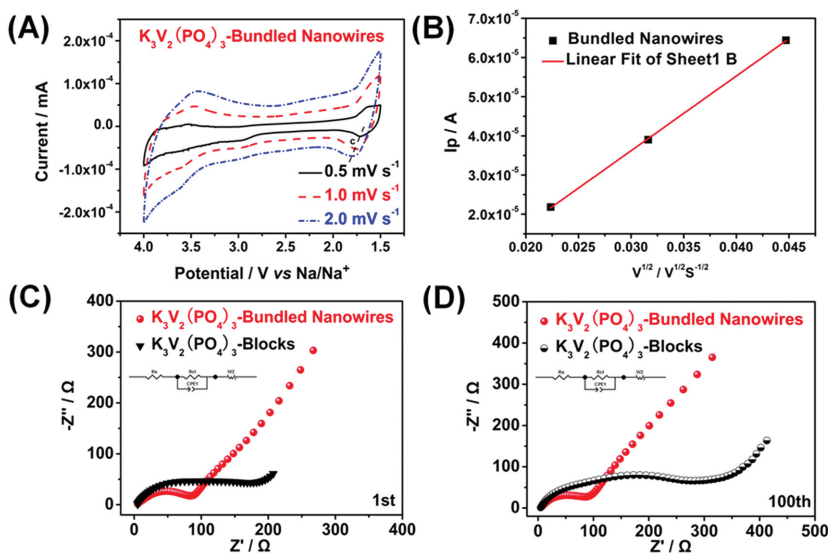


Figure 5. A) CV curves of the bundled nanowires in the electrochemical window of 1.5–4.0 V at different scan rates. B) Cycling response of the bundled nanowires analyzed by the Randles–Sevcik equation. C, D) AC plots of the bundled nanowires and blocks.

between neighboring nanowires, leading to the attractive structure stability and thus remarkable ultralong cycle life. Fourth, the bundled nanowires with large surface area ($44.0 \text{ m}^2 \text{ g}^{-1}$) provide more active sites and larger electrode–electrolyte contact area than the blocks, resulting in the excellent electrochemical performance. By combining all the above advantages, the $K_3V_2(PO_4)_3/C$ bundled nanowires demonstrate impressive electrochemical performances with outstanding cyclability and exceptional rate capability.

3. Conclusion

In summary, novel $K_3V_2(PO_4)_3/C$ bundled nanowires have been synthesized by a facile organic acid-assisted method. When used as the cathode in sodium-ion battery, the $K_3V_2(PO_4)_3/C$ nanowires exhibit an initial capacity of 119 mAh g^{-1} at 100 mA g^{-1} and a superior capacity retention of 99.0% at 1000 mA g^{-1} for 2000 cycles. The remarkable electrochemical performance is attributed to the highly stable framework, nanoporous structure, and in situ surface carbon coating. Our study demonstrates that the $K_3V_2(PO_4)_3/C$ bundled nanowire is a promising cathode material for high-performance sodium-ion battery, which is important for the development of large-scale energy storage systems. Besides, the organic acid-assisted strategy also shows great potential in the preparation and modification of other active materials for energy storage.

4. Experimental Section

Synthesis of $K_3V_2(PO_4)_3/C$ Bundled Nanowires and $K_3V_2(PO_4)_3/C$ Blocks: NH_4VO_3 , KOH, H_3PO_4 , and other chemical reagents were analytical pure and purchased from Sinopharm Chemical Reagent Co., Ltd. First, NH_4VO_3 (5.0 mmol) was dispersed in deionized water (20 mL) under vigorous stirring at $25 \text{ }^\circ\text{C}$ to obtain a white suspension. After

stirring for 10 min, KOH (7.5 mmol) was added, and the system gradually became transparent. After stirring for another 10 min, H_3PO_4 (7.5 mmol) was slowly added, and the color of the solution quickly turned into brown red. $C_2H_2O_4 \cdot 2H_2O$ (2.0 g) was then slowly added and vigorously stirred for 4 h at $25 \text{ }^\circ\text{C}$, during which the color of the solution gradually turned into yellowish green. After that, the solution was transferred into a Petri dish with a diameter of 15 cm, dried at $60 \text{ }^\circ\text{C}$, and baked at $180 \text{ }^\circ\text{C}$ for 24 h to obtain a sponge-like solid. Finally, the sponge-like solid was calcined in air at $300 \text{ }^\circ\text{C}$ for 4 h and then sintered in argon at $700\text{--}900 \text{ }^\circ\text{C}$ for 10 h with a heating rate of $5 \text{ }^\circ\text{C min}^{-1}$ to obtain the $K_3V_2(PO_4)_3/C$ bundled nanowires. As a controlled experiment, the $K_3V_2(PO_4)_3/C$ blocks were synthesized by keeping the yellowish green solution under vigorous stirring for another 8 h until the solution turned into dark blue, while the other synthesis conditions were kept unchanged.

Material Characterization: In situ X-ray diffraction experiments during electrochemical measurement of the batteries were performed on a D8 Discover X-ray diffractometer with a nonmonochromated $Cu K\alpha$ X-ray source scanned between 16° and 41° 2θ ranges. An in situ battery was designed with a Be window for X-ray penetration. Cathodes were prepared with 50% active material, 40% acetylene black, and 10% PVDF (using *N*-methyl-2-pyrrolidone solvent). 1 M $NaClO_4$ in a mixture of ethylene carbon/dimethyl carbonate (1:1 w/w) with 2.0 wt% propylene carbonate (electrolyte additive) was used as the electrolyte^[40] and Celgard 2400 microporous membrane as a separator. The cathode was then cut into square slice with $\approx 0.49 \text{ cm}^2$ in area and $\approx 0.1 \text{ mm}$ in thickness. The loading of active material is approximately $2.5\text{--}2.8 \text{ mg cm}^{-2}$. X-ray diffraction (XRD) measurements were performed to obtain the crystallographic information using a D8 Discover X-ray diffractometer with a nonmonochromated $Cu K\alpha$ X-ray source. Field emission scanning electron microscopic (FESEM) images were collected using a JEOL-7100F microscopy. Thermogravimetric-DSC analyses were conducted using a STA-449C. Energy-dispersive X-ray spectra were recorded using an Oxford IE250 system. X-ray photoelectron spectroscopy analysis was conducted on a VG Multilab 2000. Transmission electron microscopic (TEM) and HRTEM images were recorded using a JEOL JEM-2100F TEM. The BET surface area was calculated from nitrogen adsorption isotherms measured at 77 K using a Tristar-3020 instrument.

Electrochemical Measurements: The electrochemical measurements were carried out by assembly of 2016 coin cells in a glove box filled with pure argon gas, using sodium discs as both the counter electrode and the reference electrode, 1 M $NaClO_4$ in a mixture of ethylene carbon/dimethyl carbonate (1:1 w/w) with 2.0 wt% propylene carbonate (electrolyte additive) as the electrolyte,^[40] and Celgard 2400 microporous membrane as the separator. Cathodes were obtained with 70% active material, 20% acetylene black, and 10% PVDF (using *N*-methyl-2-pyrrolidone solvent). The cathode was cut into square slice with $\approx 0.49 \text{ cm}^2$ in area and $\approx 0.1 \text{ mm}$ in thickness. The loading of active material is approximately $3.5\text{--}3.9 \text{ mg cm}^{-2}$. Galvanostatic charge–discharge tests were performed at a potential range of 1.5–4.0 V versus Na/Na⁺ using a multichannel battery testing system (LAND CT2001A). Cyclic voltammetry (CV) and electrochemical impedance spectra (EIS) were tested with an electrochemical workstation (Autolab PGSTAT 302N and CHI600E).

Supporting Information

Supporting Information is available from the Wiley Online Library or from the author.

Acknowledgements

X.W., C.N., and J.M. contributed equally to this work. This work was supported by the National Basic Research Program of China (2013CB934103, 2012CB933003), the International Science and Technology Cooperation Program of China (2013DFA50840), the National Natural Science Foundation of China (51272197, 51302203), the Fundamental Research Funds for the Central Universities (2014-VII-007, 2014-IV-083, 2014-ZY-016), Hubei Collaborative Innovation Center for Automotive Components Technology (WUT), Hubei Province Natural Science Fund for Distinguished Young Scholars (2014CFA035), and the Students Innovation and Entrepreneurship Training Program (2014-CL-A1-01, 20141049701008). The authors thank Prof. C. M. Lieber of Harvard University, Prof. D. Y. Zhao of Fudan University for strong support and stimulating discussions. The authors also thank the Center for Materials Research and Analysis from Wuhan University of Technology.

Received: April 11, 2015

Revised: May 29, 2015

Published online:

- [1] Z. G. Yang, J. L. Zhang, M. C. W. Kintner-Meyer, X. C. Lu, D. Choi, J. P. Lemmon, J. Liu, *Chem. Rev.* **2011**, *111*, 3577.
- [2] B. Dunn, H. Kamath, J.-M. Tarascon, *Science* **2011**, *334*, 928.
- [3] M. Armand, J.-M. Tarascon, *Nature* **2008**, *451*, 652.
- [4] S. Y. Hong, Y. Kim, Y. Park, A. Choi, N.-S. Choi, K. T. Lee, *Energy Environ. Sci.* **2013**, *6*, 2067.
- [5] V. Palomares, P. Serras, I. Villaluenga, K. B. Hueso, J. Carretero-Gonzalez, T. Rojo, *Energy Environ. Sci.* **2012**, *5*, 5884.
- [6] H. L. Pan, Y.-S. Hu, L. Q. Chen, *Energy Environ. Sci.* **2013**, *6*, 2338.
- [7] M. D. Slater, D. Kim, E. Lee, C. S. Johnson, *Adv. Funct. Mater.* **2013**, *23*, 947.
- [8] S.-W. Kim, D.-H. Seo, X. H. Ma, G. Ceder, K. Kang, *Adv. Funct. Mater.* **2012**, *7*, 710.
- [9] L. Wang, Y. H. Lu, J. Liu, M. W. Xu, J. G. Cheng, D. W. Zhang, J. B. Goodenough, *Angew. Chem. Int. Ed.* **2013**, *52*, 1.
- [10] L. B. Hu, F. La Mantia, H. Wu, X. Xie, J. McDonough, M. Pasta, Y. Cui, *Adv. Energy Mater.* **2011**, *1*, 1012.
- [11] S. Li, Y. F. Dong, L. Xu, X. Xu, L. He, L. Q. Mai, *Adv. Mater.* **2014**, *26*, 3545.
- [12] Y. Liu, Y. Qiao, W. X. Zhang, H. H. Xu, Z. Li, Y. Shen, L. X. Yuan, X. L. Hu, X. Dai, Y. H. Huang, *Nano Energy* **2014**, *5*, 97.
- [13] L. Q. Mai, X. C. Tian, X. Xu, L. Chang, L. Xu, *Chem. Rev.* **2014**, *114*, 11828.
- [14] R. Hao, R. J. Xing, Z. C. Xu, Y. L. Hou, S. Gao, S. H. Sun, *Adv. Mater.* **2010**, *22*, 2729.
- [15] V. Raju, J. Rains, C. Gates, W. Luo, X. F. Wang, W. F. Stickley, G. D. Stucky, X. L. Ji, *Nano Lett.* **2014**, *14*, 4119.
- [16] J. Tang, Y. Y. Zhang, B. Kong, Y. C. Wang, P. M. Da, J. Li, A. A. Elzatahry, D. Y. Zhao, X. G. Gong, G. F. Zheng, *Nano Lett.* **2014**, *14*, 2702.
- [17] J. Chen, L. Xu, W. Y. Li, X. L. Gou, *Adv. Mater.* **2005**, *17*, 582.
- [18] Z. Li, Y. M. Huang, L. X. Yuan, Z. X. Hao, Y. H. Huang, *Carbon* **2015**, *92*, 41.
- [19] C. J. Niu, J. S. Meng, X. P. Wang, C. H. Han, M. Y. Yan, K. N. Zhao, X. M. Xu, W. H. Ren, Y. L. Zhao, L. Xu, Q. J. Zhang, D. Y. Zhao, L. Q. Mai, *Nat. Commun.* **2015**, *6*, 7402.
- [20] Q. L. Wei, Q. Y. An, D. D. Chen, L. Q. Mai, S. Y. Chen, Y. L. Zhao, K. M. Hercule, L. Xu, A. Minhas-Khan, Q. J. Zhang, *Nano Lett.* **2014**, *14*, 1042.
- [21] S.-C. Yin, H. Grondey, P. Strobel, M. Anne, L. F. Nazar, *J. Am. Chem. Soc.* **2003**, *125*, 10402.
- [22] S. Y. Lim, H. Kim, R. A. Shakoob, Y. Jung, J. W. Choi, *J. Electrochem. Soc.* **2012**, *159*, A1393.
- [23] Z. L. Jian, L. Zhao, H. L. Pan, Y.-S. Hu, H. Li, W. Chen, L. Q. Chen, *Electrochem. Commun.* **2012**, *14*, 86.
- [24] Q. Q. Chen, X. C. Qiao, Y. B. Wang, T. T. Zhang, C. Peng, W. M. Yin, L. Liu, *J. Power Sources* **2012**, *201*, 267.
- [25] K. Saravanan, C. W. Mason, A. Rudola, K. H. Wong, P. Balaya, *Adv. Energy Mater.* **2013**, *3*, 444.
- [26] J. Gopalakrishnan, K. K. Rangan, *Chem. Mater.* **1992**, *4*, 745.
- [27] A. Corma, F. Rey, J. Rius, M. J. Sabater, S. Valencia, *Nature* **2004**, *431*, 287.
- [28] D. W. Lewis, D. J. Willock, C. R. A. Catlow, J. M. Thoms, G. J. Hutchings, *Nature* **1996**, *382*, 604.
- [29] C. J. Niu, J. S. Meng, C. H. Han, K. N. Zhao, M. Y. Yan, L. Q. Mai, *Nano Lett.* **2014**, *14*, 2873.
- [30] N. Gokulakrishnan, A. Pandurangan, P. K. Sinha, *Ind. Eng. Chem. Res.* **2009**, *48*, 1556.
- [31] P. Lespadea, *Carbon* **1982**, *20*, 427.
- [32] A. C. Ferrari, J. Robertson, *Phys. Rev. B: Condens. Matter* **2000**, *61*, 14095.
- [33] A. Janes, T. Thornberg, H. Kurig, E. Lust, *Carbon* **2009**, *47*, 23.
- [34] X. L. Wu, L. Y. Jiang, F. F. Cao, Y. G. Guo, L. J. Wan, *Adv. Mater.* **2009**, *21*, 2710.
- [35] J. R. Ferraro, A. Walker, *J. Chem. Phys.* **1965**, *42*, 1278.
- [36] C. Ohtsuki, T. Kokubo, T. Yamamuro, *J. Non-Cryst. Solids* **1992**, *143*, 84.
- [37] E. J. Baran, P. J. Aymonino, *Acta A: Mol. Spectrosc.* **1968**, *24*, 291.
- [38] G. Silversmit, D. Depla, H. Poelman, G. B. Marin, R. De Gryse, *J. Electron. Spectrosc.* **2004**, *135*, 167.
- [39] B. S. Liu, X. L. Wang, G. F. Cai, L. P. Wen, Y. B. Song, X. J. Zhao, *J. Hazard. Mater.* **2009**, *169*, 1112.
- [40] M. W. Song, M. Kang, K. L. Kim, *React. Kinet. Catal. Lett.* **2003**, *78*, 365.
- [41] H. Liu, F. C. Strohbridge, O. J. Borkiewicz, K. M. Wiaderek, K. W. Chapman, P. J. Chupas, C. P. Grey, *Science* **2014**, *344*, 1451.
- [42] S. Nasri, M. Megdiche, M. Gargo, *Phys. B* **2014**, *451*, 120.
- [43] B. E. Warren, *Google*, **1902**, Ch. 4.
- [44] D. Schryvers, G. S. Firstov, J. W. Seo, J. Van Humbeeck, Y. N. Koval, *Scr. Mater.* **1997**, *36*, 1119.
- [45] C. M. Julien, M. Massot, C. Poincignon, *Spectrochim. Acta A* **2004**, *60*, 689.
- [46] M. R. Babaa, I. Stepanek, K. Masenelli-Varlot, N. Dupont-Pavlovsky, E. McRae, P. Bernier, *Surf. Sci.* **2003**, *531*, 86.
- [47] X. L. Zhang, F. Y. Cheng, J. G. Yang, J. Chen, *Nano Lett.* **2013**, *13*, 2822.
- [48] C. Luo, Y. H. Xu, Y. J. Zhu, Y. H. Liu, S. Y. Zheng, Y. Liu, A. Langrock, C. S. Wang, *ACS Nano* **2013**, *7*, 8003.
- [49] H.-G. Jung, J. Hassoun, J.-B. Park, Y.-K. Sun, B. Scrosat, *Nat. Chem.* **2012**, *4*, 579.

ADVANCED ENERGY MATERIALS

Supporting Information

for *Adv. Energy Mater.*, DOI: 10.1002/aenm.201500716

Novel $K_3V_2(PO_4)_3/C$ Bundled Nanowires as Superior Sodium-Ion Battery Electrode with Ultrahigh Cycling Stability

*Xuanpeng Wang, Chaojiang Niu, Jiashen Meng, Ping Hu, Xiaoming Xu, Xiujuan Wei, Liang Zhou, * Kangning Zhao, Wen Luo, Mengyu Yan, and Liqiang Mai**

Supporting Information

Novel $K_3V_2(PO_4)_3/C$ bundled nanowires as superior sodium-ion battery electrode with ultra-high cycling stability

Xuanpeng Wang[†], Chaojiang Niu[†], Jiashen Meng[†], Ping Hu, Xiaoming Xu, Xiujuan Wei, Liang Zhou*, Kangning Zhao, Wen Luo, Mengyu Yan and Liqiang Mai*

[†]These authors contributed equally to this work.

X.P. Wang, C. J. Niu, J. S. Meng, P. Hu, X. M. Xu, X. J. Wei, K. N. Zhao, W. Luo, M.

Y. Yan, Prof. L. Zhou, Prof. L. Q. Mai

State Key Laboratory of Advanced Technology for Materials Synthesis and

Processing, Wuhan University of Technology

Wuhan 430070, China

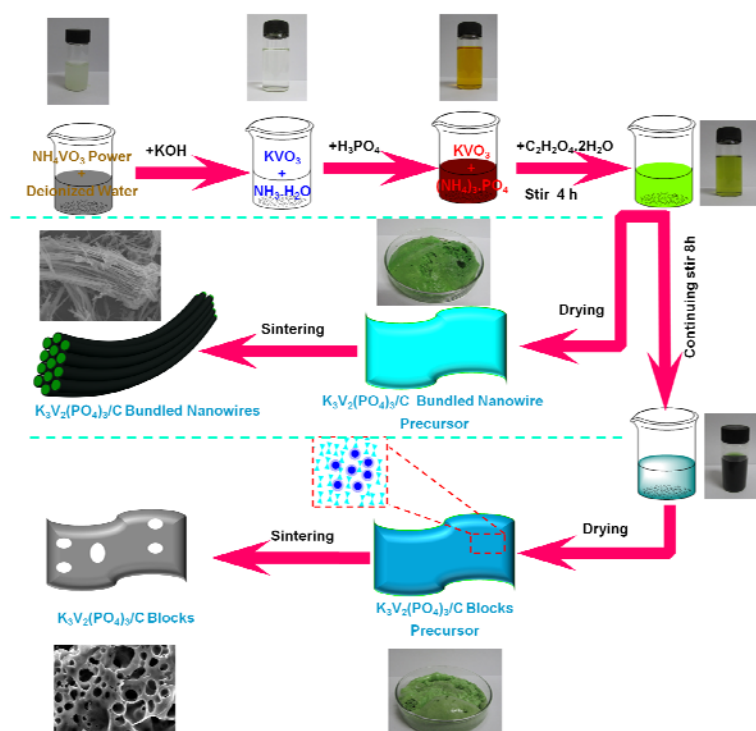


Figure S1. Schematic illustration for the fabrication process and proposed formation mechanism of the $K_3V_2(PO_4)_3/C$ bundled nanowires and blocks.

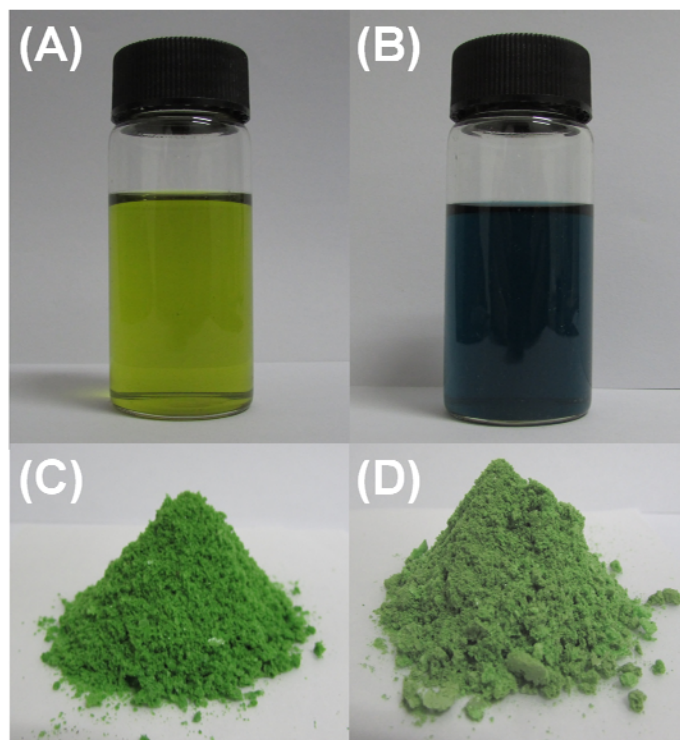


Figure S2. The photos for solution precursor of $\text{K}_3\text{V}_2(\text{PO}_4)_3$ bundled nanowires (A) and blocks (B). The photos for dried precursor of $\text{K}_3\text{V}_2(\text{PO}_4)_3$ bundled nanowires (C) and blocks (D).

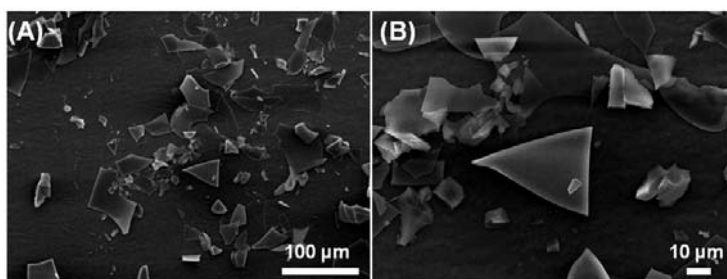


Figure S3. (A, B) SEM images of the $\text{K}_3\text{V}_2(\text{PO}_4)_3$ precursor baked at 180°C for 2h.

Table S1. The ICP test results of the $\text{K}_3\text{V}_2(\text{PO}_4)_3/\text{C}$ bundled nanowires.

Temperature	K: V: P
700 °C	3.0 : 2.04 : 2.97
800 °C	3.0 : 2.06 : 3.04
900 °C	3.0 : 1.99 : 3.08

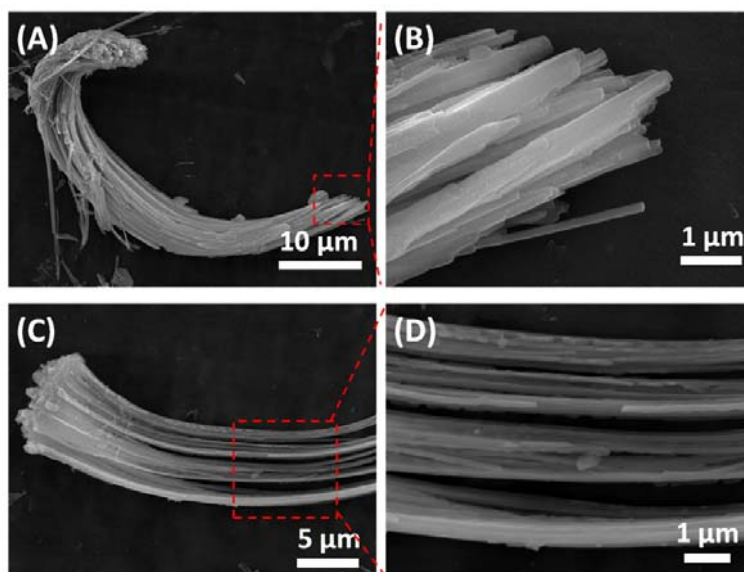


Figure S4. SEM images of the $\text{K}_3\text{V}_2(\text{PO}_4)_3/\text{C}$ bundled nanowires sintered at 800 °C.

Table S2. The ICP test results of the $\text{K}_3\text{V}_2(\text{PO}_4)_3/\text{C}$ blocks sintered at 800 °C.

	Temperature	K: V: P
Blocks	800 °C	3.00 : 2.03 : 3.01

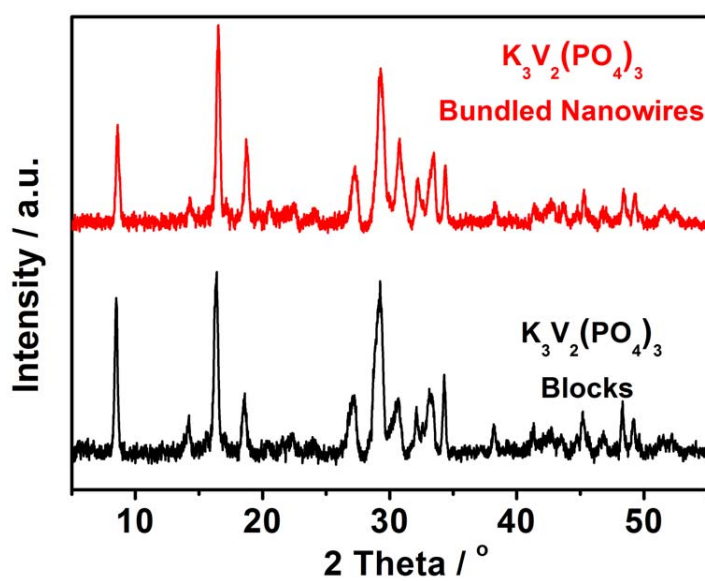


Figure S5. XRD patterns of the $\text{K}_3\text{V}_2(\text{PO}_4)_3/\text{C}$ bundled nanowires and blocks sintered at 800 °C.

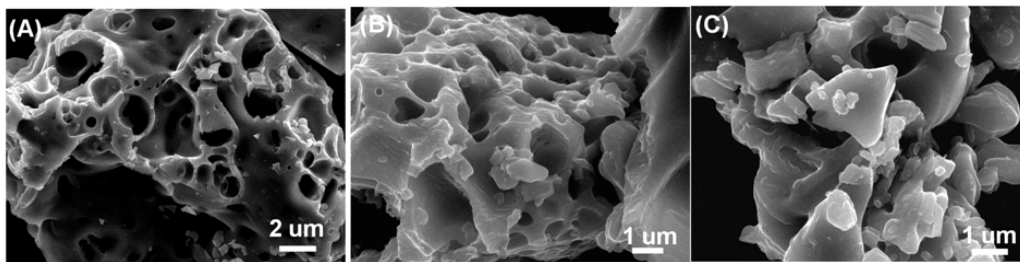


Figure S6. (A-C) SEM images of the $\text{K}_3\text{V}_2(\text{PO}_4)_3/\text{C}$ blocks sintered at 800 °C.

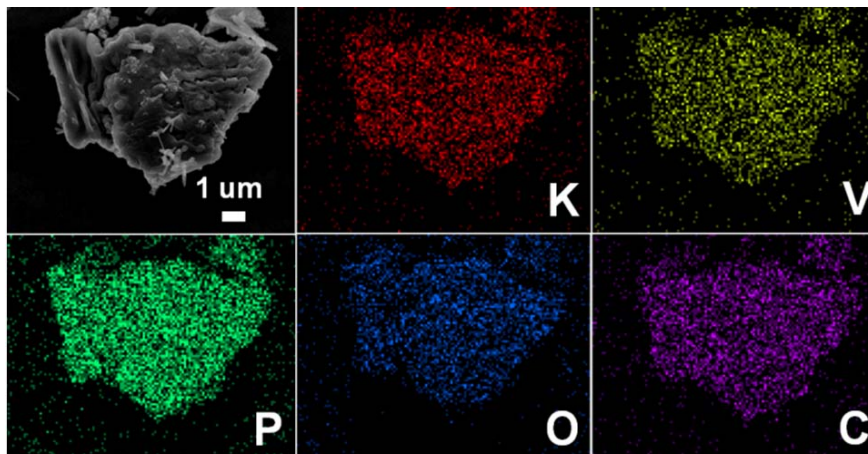


Figure S7. Elemental mapping images of the $\text{K}_3\text{V}_2(\text{PO}_4)_3/\text{C}$ blocks sintered at 800 °C.

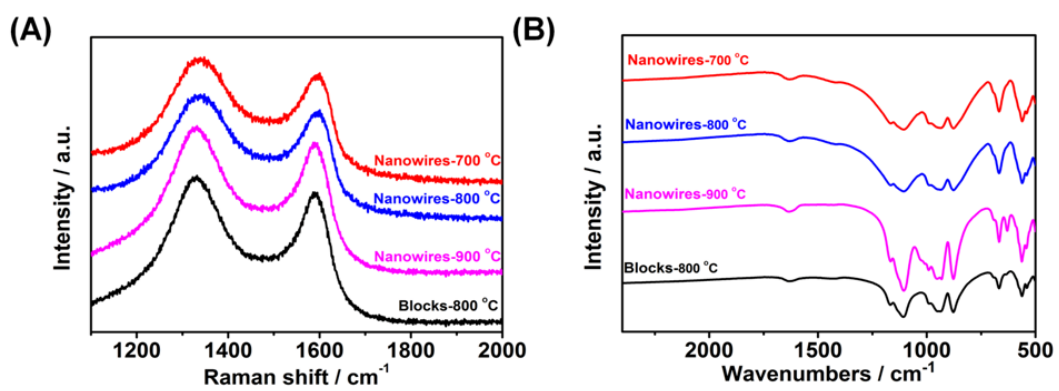


Figure S8. Raman spectra (A) and FT-IR spectra (B) of the $\text{K}_3\text{V}_2(\text{PO}_4)_3/\text{C}$ samples.

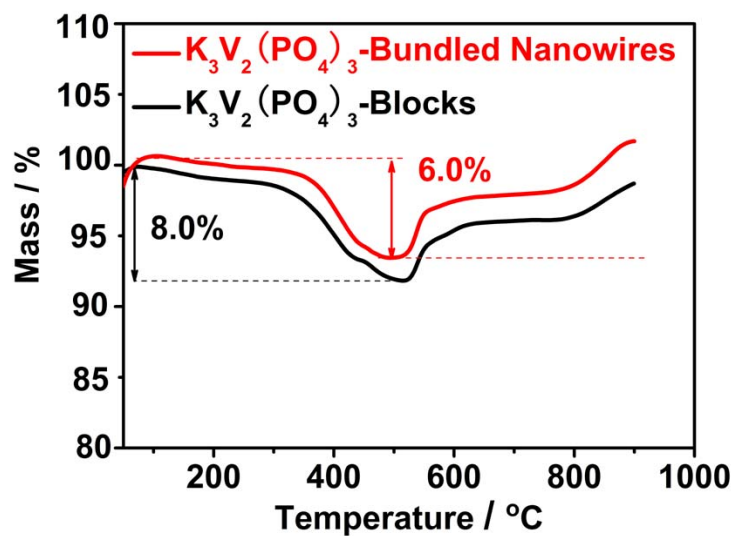


Figure S9. TGA curves of the $\text{K}_3\text{V}_2(\text{PO}_4)_3/\text{C}$ bundled nanowires and blocks sintered at $800\text{ }^\circ\text{C}$.

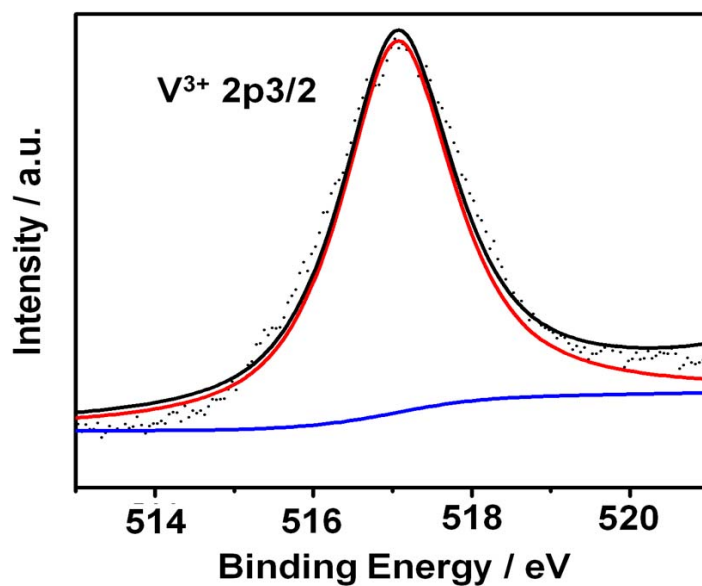


Figure S10. XPS spectra of the $\text{V } 2p_{3/2}$ core level region of the $\text{K}_3\text{V}_2(\text{PO}_4)_3/\text{C}$ bundled nanowires.

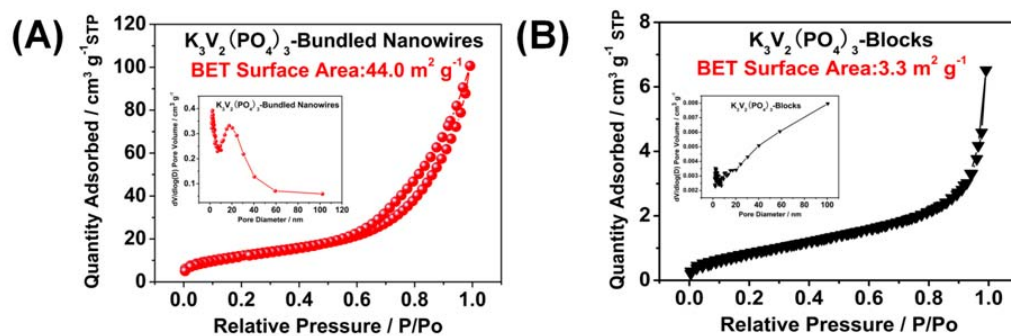


Figure S11. The nitrogen adsorption-desorption isotherms of the $K_3V_2(PO_4)_3/C$ bundled nanowires (A) and blocks (B). The pore size distribution of the $K_3V_2(PO_4)_3/C$ bundled nanowires (inset of A) and blocks (inset of B).

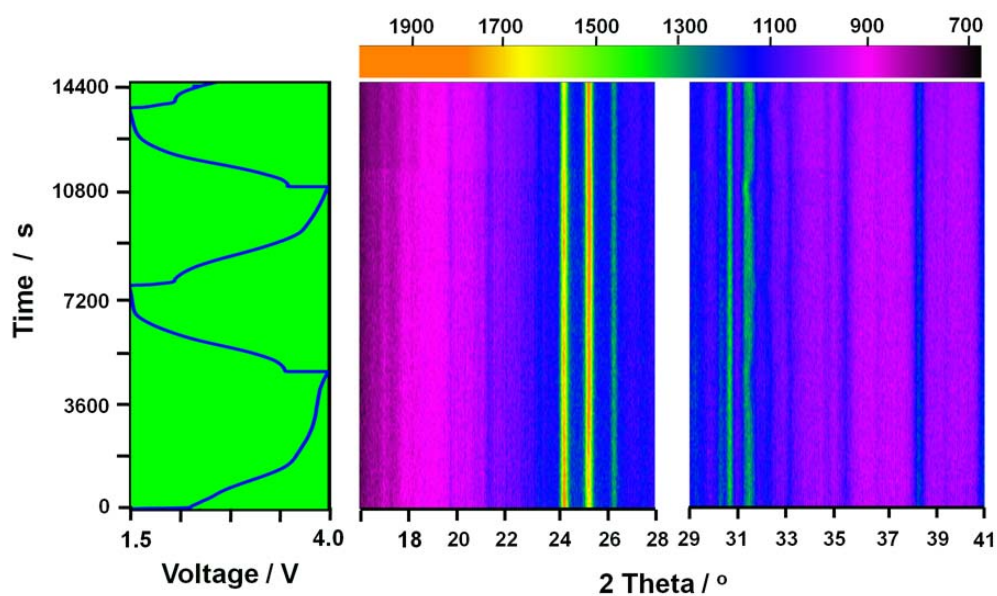


Figure S12. *In situ* X-ray diffraction patterns during galvanostatic charge and discharge of the $K_3V_2(PO_4)_3/C$ bundled nanowires at 100 mA g^{-1} .

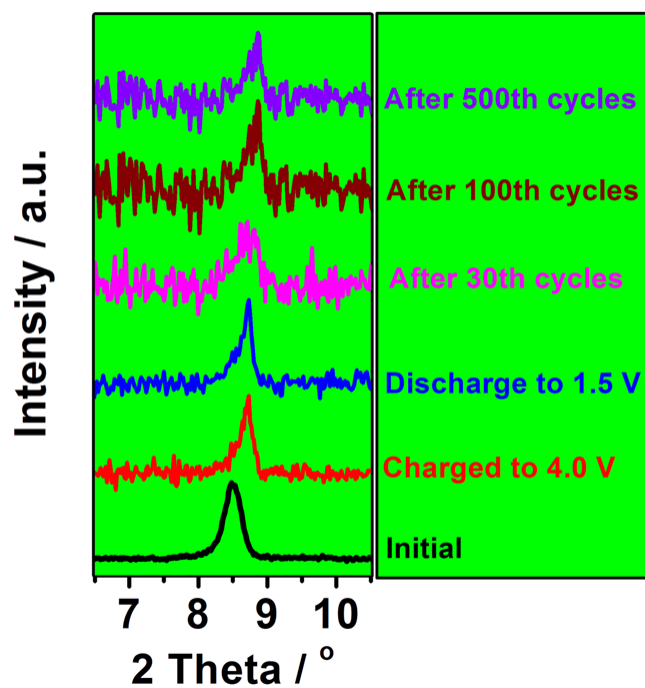


Figure S13. *Ex situ* XRD patterns of the $K_3V_2(PO_4)_3/C$ bundled nanowires.

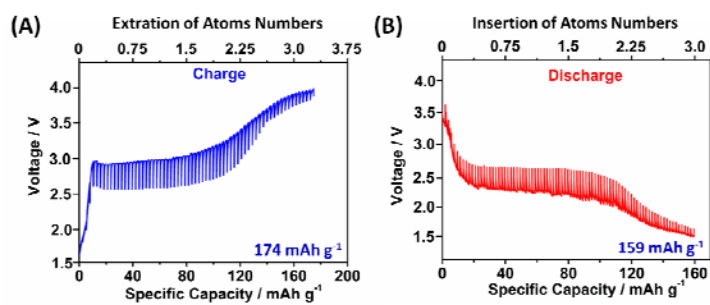


Figure S14. The galvanostatic intermittent titration technique (GITT) for $K_3V_2(PO_4)_3$ bundled nanowires.

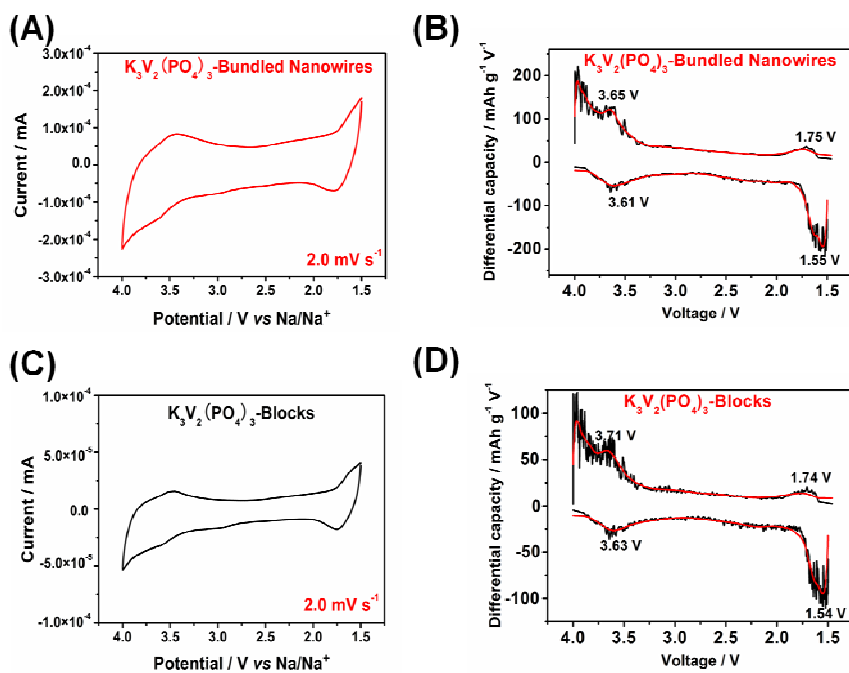


Figure S15. Cyclic voltammograms (CV) and corresponding dq/dv plots of the $K_3V_2(PO_4)_3/C$ bundled nanowires (A and B) and blocks (C and D) at a scan rate of 2.0 mV s⁻¹ in the electrochemical window of 1.5 to 4.0 V vs. Na/Na⁺.

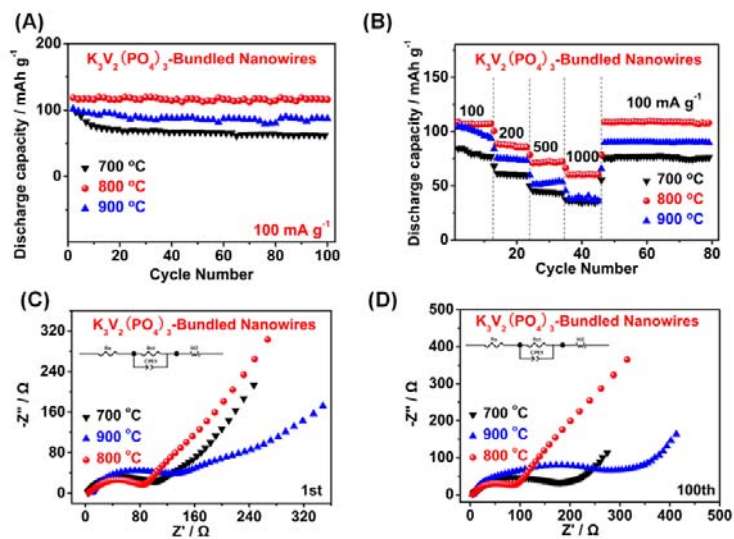


Figure S16. (A) Cycling performance of the three $K_3V_2(PO_4)_3/C$ bundled nanowires at 100 mA g⁻¹ in the electrochemical window of 1.5 – 4.0 V. (B) Rate performance of the three samples. (C, D) AC impedance plots of the three samples before and after 100th cycles (from 0.1Hz to 100 kHz).

Table S3. The *ex situ* ICP test results of the $\text{K}_3\text{V}_2(\text{PO}_4)_3/\text{C}$ bundled nanowires.

	K: Na: V
Before cycle	3.02 : 0.81 : 2.00
Charge to 4.0 V	1.01 : 0.01 : 2.00
Discharge to 1.5 V	1.16 : 2.10 : 2.00
After 2 cycles	1.07 : 2.26 : 2.00
After 30 cycles	1.02 : 2.25 : 2.00
After 100 cycles	1.01 : 2.24 : 2.00
After 500 cycles	1.02 : 2.25 : 2.00

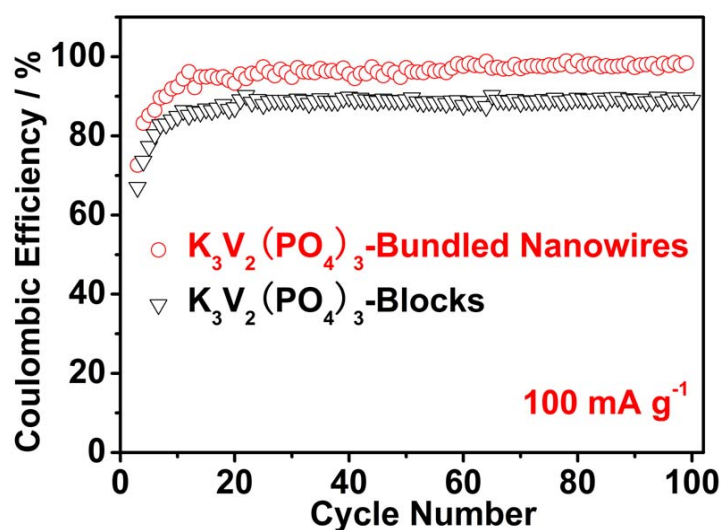


Figure S17. Coulombic efficiency of the $\text{K}_3\text{V}_2(\text{PO}_4)_3/\text{C}$ bundled nanowires and blocks at 100 mA g^{-1} .

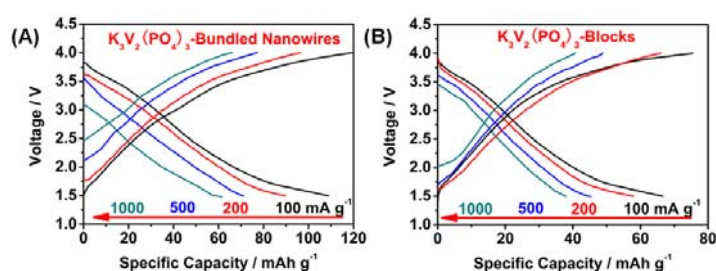


Figure S18. Charge-discharge curves of the $\text{K}_3\text{V}_2(\text{PO}_4)_3/\text{C}$ bundled nanowires (A) and blocks (B), at various current densities from 100 to $1,000 \text{ mA g}^{-1}$.

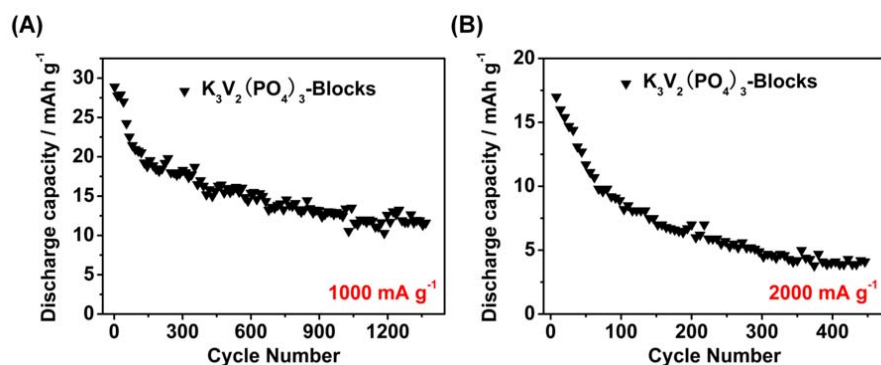


Figure S19. The cycle performances of the $K_3V_2(PO_4)_3/C$ blocks at 1,000 (A) and 2,000 $mA\ g^{-1}$ (B).

Table S4. Comparison of the electrochemical performance of phosphate based electrodes for sodium-ion batteries.

Material	Current density ($mA\ g^{-1}$)	Initial capacity ($mAh\ g^{-1}$)	Cycle numbers	Per cycle decay (%)	Reference
1 $K_3V_2(PO_4)_3$	100	119	100	0.0213	Our work
	500	71.0	1,000	0.0026	
	1,000	66.0	2,000	0.0023	
	2,000	45.7	2,000	0.0016	
2	588	100.6	200	0.0015	S1
3	1,176	103	1,000	0.0029	S2
4	4,700	60	30,000	0.013	S3
5 $Na_3V_2(PO_4)_3$	1,176	86	300	0.023	S4
6	11.76	109	80	0.088	S5
7	588	95	700	0.0056	S6
8	5.88	50	50	0.146	S7

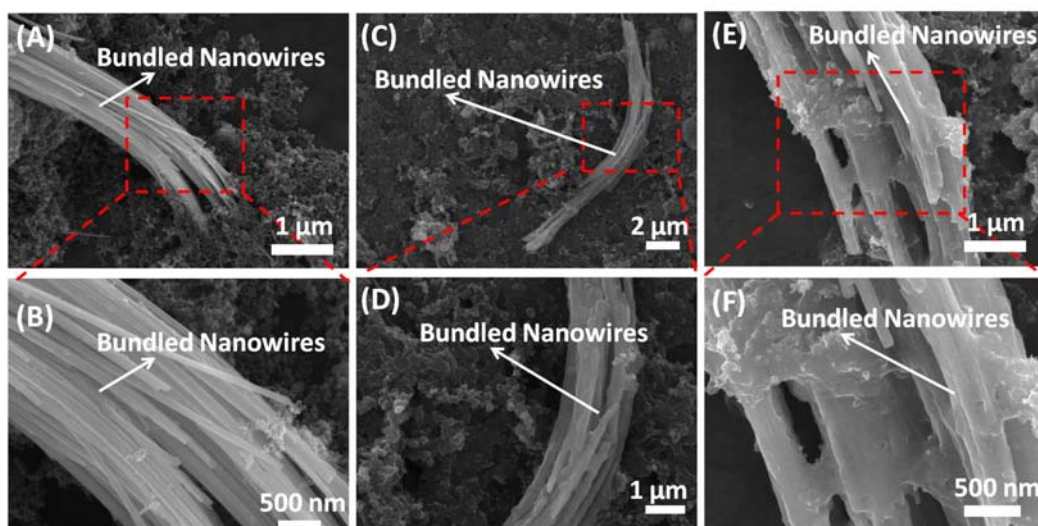


Figure S20. SEM images of the $\text{K}_3\text{V}_2(\text{PO}_4)_3/\text{C}$ bundled nanowires before cycling (A, B), after 100 cycles at 100 mA g^{-1} (C, D), and after 2,000 cycles at $1,000 \text{ mA g}^{-1}$ (E, F).

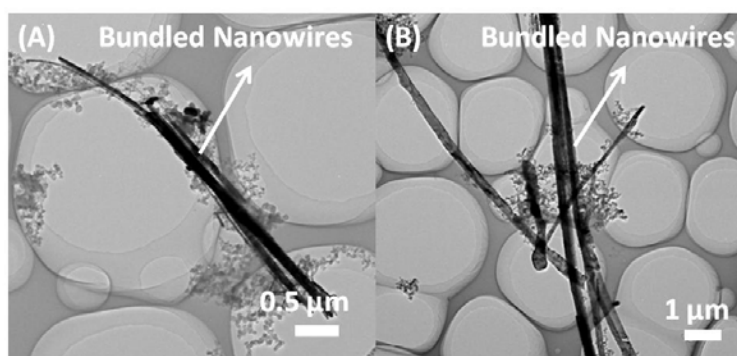


Figure S21. (A, B) TEM images of the $\text{K}_3\text{V}_2(\text{PO}_4)_3/\text{C}$ bundled nanowires after 100 cycles at 100 mA g^{-1} .

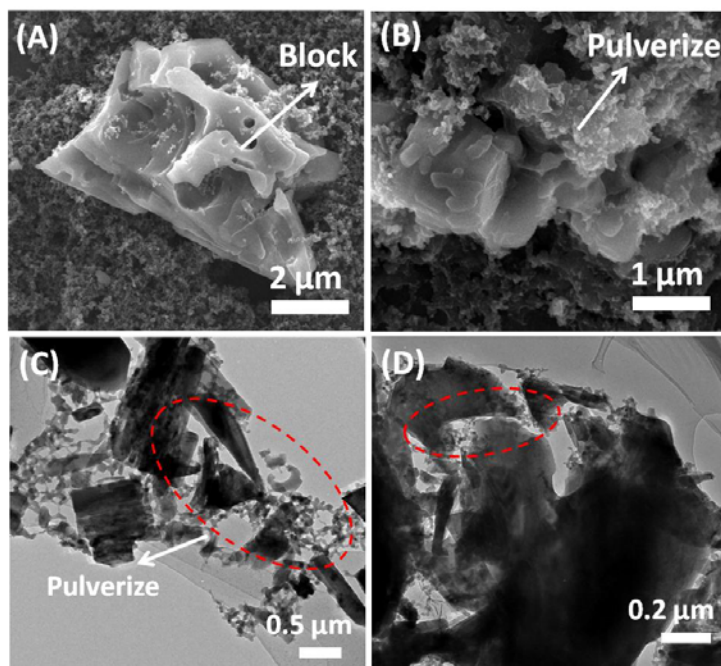


Figure S22. SEM images of the $\text{K}_3\text{V}_2(\text{PO}_4)_3/\text{C}$ blocks before cycling (A) and after 100 cycles at 100 mA g^{-1} (B). TEM images of the $\text{K}_3\text{V}_2(\text{PO}_4)_3/\text{C}$ blocks after 100 cycles at 100 mA g^{-1} (C, D).

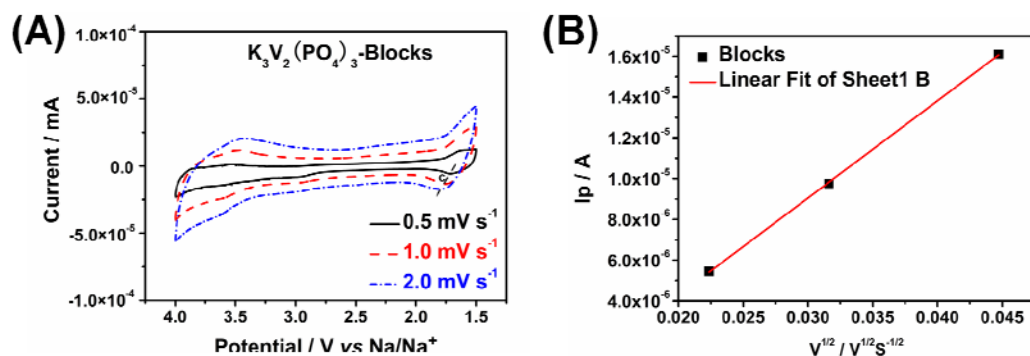


Figure S23. (A) CV curves of the $\text{K}_3\text{V}_2(\text{PO}_4)_3/\text{C}$ blocks in the electrochemical window of 1.5 – 4.0 V at different scan rates. (B) Cycling response of the $\text{K}_3\text{V}_2(\text{PO}_4)_3/\text{C}$ blocks analyzed by the Randles-Sevick equation.

Reference

- S1. S. Li, Y. F. Dong, L. Xu, X. Xu, L. He, L. Q. Mai, *Adv. Mat.* **2014**, 26, 3545.
 S2. C. B. Zhu, K. P. Song, Peter A. van Aken, J. Maier, Y. Yu, *Nano Lett.* **2014**, 14, 2175.
 S3. K. Saravanan, C. W. Mason, A. Rudola, K. H. Wong, P. Balaya, *Adv. Energy. Mater.* **2013**, 3, 444.
 S4. Y. H. Jung, C. H. Lim, D. K. Kim, *J. Mater. Chem. A* **2013**, 1, 11350.
 S5. Z. L. Jian, W. Z. Han, X. Lu, H. X. Yang, Y. S. Hu, J. Zhou, Z. B. Zhou, J. Q. Li, W. Chen, D. F. Chen, L. Q. Chen, *Adv. Energy Mater.* **2013**, 3, 156.
 S6. W. C. Duan, Z. Q. Zhu, H. Li, Z. Hu, K. Zhang, F. Y. Cheng, J. Chen, *J. Mater. Chem. A* **2014**, 2, 8668.
 S7. W. Shen, C. Wang, H. M. Liu, W. S. Yang, *Chem. -Eur. J.* **2013**, 19, 14712.